Applied Catalysis B: Environmental 144 (2014) 269–276

Contents lists available at ScienceDirect

Applied Catalysis B: Environmental

journal homepage: www.elsevier.com/locate/apcatb

Influence of iron leaching and oxidizing agent employed on solar photodegradation of phenol over nanostructured iron-doped titania catalysts

C. Adán[a], A. Bahamonde[a], I. Oller[b], S. Malato[b], A. Martínez-Arias[a,*]

[a] Instituto de Catálisis y Petroleoquímica, CSIC, C/Marie Curie 2, Cantoblanco, 28049 Madrid, Spain
[b] Plataforma Solar de Almería-CIEMAT, Ctra. de Senés s/n, 04200 Tabernas, Almería, Spain

ARTICLE INFO

Article history:
Received 8 May 2013
Received in revised form 8 July 2013
Accepted 11 July 2013
Available online 19 July 2013

Keywords:
Solar photocatalysis
Iron leaching
Phenol
Fe–TiO_2
H_2O_2

ABSTRACT

Iron-doped TiO_2 catalysts with two different iron contents (0.7 and 3.5 wt.%) as well as the corresponding undoped system, prepared by a combined sol–gel/microemulsion method and calcined at 600 °C, have been examined with respect to their behaviour for photocatalytic degradation of aqueous phenol with H_2O_2 under solar light. The activity results are complemented with structural/morphological and electronic characterization analysis achieved by XRD, TEM, Raman, S_{BET}, UV–vis DRS and XPS techniques. A detrimental effect of the presence of iron on the photoactivity is detected for the sample with 0.7 wt.% iron. In contrast, some activity enhancement is produced for the sample with highest iron loading. Such irregular catalytic behaviour with respect to iron loading is analyzed on the basis of the presence of additional catalytic contributions from new photoactive species. These are created as a consequence of surface modifications produced under reaction conditions related to the existence of phenomena of iron leaching from the catalysts. Differences in the specific nanostructure present in each case can also play a role on explaining the differences observed in the photoactivity. Finally, an analysis of the photoactivity as a function of the oxidizing agent employed, either H_2O_2 or oxygen from air, is also performed.

1. Introduction

Polycrystalline titanium dioxide presents unique properties as heterogeneous photocatalyst considering its good stability in aqueous environment under ambient pressure and temperature condition [1,2]. However, its photocatalytic efficiency can be limited by stabilization of the charge photocarriers in the bulk of the material, by fast electron–hole recombination either at the bulk or at the surface of the oxide or by its relatively large band gap which limits light absorption in the visible region [1–6]. Among strategies aimed to enhance such properties, in particular extending light absorption to the visible region, it is common to employ methods based on doping the titania catalyst with transition metal cations [7–10]. Fe^{3+} is considered among most interesting dopants in this sense since it originates a localized narrow band above the valence band of titania which makes the catalyst sensitive to visible absorption [11,12]. However, the catalytic role of the Fe^{3+} dopant during photooxidation processes remains controversial [8–10,13–15]. Thus, discrepancies appear with respect to its role in enhancing electron/hole recombination properties since the presence of iron in the catalyst formulation has been reported to be detrimental to the photoactivity in a great number of cases [10,13]. In turn, the photoactivity of iron-doped titania under visible light can be limited because the oxidizing power and mobility of holes in the Fe^{3+}-derived localized narrow band can be lower than that of holes in the valence band of TiO_2 [11].

In any case, optimum photocatalytic properties have been apparently achieved in an important number of cases upon homogeneous doping at a relatively low level around 0.5–1 at.%, at which the distance between dopant cations in the titania lattice could optimize dynamical characteristics of the recombination process [1,3,10]. However, doping above such optimum level typically results detrimental to the photoactivity [10,15–17]. In turn, the specific reaction conditions (solution pH or type of oxidant employed) can strongly affect the photocatalytic properties of titania-based materials [10,18,19]. In this sense, it is generally concluded that the use of H_2O_2 as oxidizing agent can significantly enhance, as compared with dissolved oxygen, the UV- or visible-photoassisted contaminants oxidation rate [18,20–22], in spite of its possible hydroxyl radical scavenger role [18,23,24]. Other interrelated aspects that could affect the photoactivity concern modifications of the surface properties induced by doping as well as the possibility that species originated from iron lixiviates can participate in the reaction mechanism [11,12,17,25–28].

* Corresponding author. Tel.: +34 915854940; fax: +34 915854760.
E-mail address: amartinez@icp.csic.es (A. Martínez-Arias).

0926-3373/$ – see front matter © 2013 Elsevier B.V. All rights reserved.
http://dx.doi.org/10.1016/j.apcatb.2013.07.027

With respect to this latter, we have proposed in a recent work the involvement of iron species leached under reaction conditions from iron-doped titania in the mechanism of solar contaminants photodegradation employing oxygen as oxidant under semi-pilot plant conditions [27]. A similar study has been performed when H_2O_2 is employed as oxidant over nanostructured anatase TiO_2 (crystal size between about 10 and 12 nm, as obtained when using calcination at 450 °C as final preparation step) systems of this kind, also indicating an important role of such leached iron species [17]. The present work aims to extend the latter analysis, employing H_2O_2 as oxidant, to more crystalline catalysts (obtained by calcination at 600 °C) in order to explore whether the mechanism involving iron leached species could still prevail in the presence of more crystallized and likely more stable iron oxide and titania entities, and considering also the effects of crystallinity on phenol photooxidation activity [22,27–30]. In this respect, it must be noted that our previous results comparing samples calcined at 450 °C (anatase) and 600 °C (mixed anatase–rutile) when using O_2 (from air) as oxidant showed a generally higher photoactivity for the latter despite their appreciably lower specific surface area [27]. Within this context, pure titania and iron-doped titania catalysts prepared by sol–gel/microemulsion method and (as final preparation step) calcined at 600 °C have been tested for phenol photodegradation with H_2O_2 under solar light irradiation in a pilot plant system. Information achieved by employing different structural and electronic characterization techniques (XRD, TEM, Raman, S_{BET}, as well as UV–vis and XPS spectroscopies) has been employed to complement the discussion of the catalytic activity results.

2. Experimental

Iron-doped photocatalysts were prepared using a combined sol–gel/microemulsion preparation method. Titanium-tetraisopropoxide was added to a reverse microemulsion in which the aqueous phase contains a solution of iron (III) nitrate nonahydrate; this was dispersed in *n*-heptane, using Triton X-100 (Aldrich) as surfactant and 1-hexanol as cosurfactant [3,15,27]. The resulting mixture was stirred for 24 h, centrifuged and decanted, and the obtained solid was rinsed with methanol and dried at room temperature for 12 h. Then, it was calcined for 2 h at 600 °C under air atmosphere. Nominal iron amounts employed (0.7 and 3.5 wt.%, corresponding to ca. 1 and 5 at.%, respectively) were similar (within experimental error) to experimental contents determined by ICP-OES chemical analysis. Reference undoped TiO_2 was prepared by using the same method. Hereafter, the catalysts will be referred to as 600-T0, 600-T1 and 600-T5; the nomenclature is the same as employed in our previous report [27] and reflects the calcination temperature employed for the preparation (prefix) and the iron at.% loading of the catalysts (suffix).

Powder XRD patterns were obtained with a Siemens D-500 apparatus using nickel-filtered Cu Kα radiation operating at 40 kV and 40 mA, with a 0.04° step size and accumulating a total of 5 s per point. Crystal size analysis was made by employing the Scherrer equation. The phase contents of a determinate catalyst were calculated from the integrated intensities of anatase (1 0 1) and rutile (1 1 0) peaks, employing a method reported elsewhere [31]. High resolution transmission electron microscopy (TEM) images were obtained with a JEOL JEM 2100F UHR electron microscope. Specimens were prepared by depositing particles of the catalysts to be investigated from acetone dispersions onto a copper grid supporting a perforated carbon film. Particle size distribution for estimation of average size has been performed by taking into account more than one hundred particles from the multiple TEM images made. Raman data were acquired using a Renishaw dispersive system 1000, equipped with a single monochromator, a holographic notch filter, and a cooled TCD; the catalysts were excited using the 514 nm emission line of an Ar laser. The diffuse reflectance absorption spectra of the photocatalysts were recorded with a UV–Visible Varian 2300 apparatus. Nitrogen adsorption–desorption isotherms (for determination of specific surface areas, as examined by the BET method) were measured at −196 °C in a Micromeritics Tristar automatic apparatus on catalysts previously outgassed overnight at 140 °C to a vacuum of $<10^{-4}$ Pa to ensure a dry clean surface free from any loosely held adsorbed species. X-ray photoelectron spectroscopy (XPS) studies were performed with a VG Escalab 200R spectrometer employing an Mg Kα (1253.6 eV) X-ray source. The catalyst was first placed in a copper holder mounted on a sample-rod in the pre-treatment chamber of the spectrometer and then outgassed at room temperature for 1 h before being transferred to the analysis chamber. The desired region of the spectrum was then scanned a number of times in order to obtain a good signal to noise ratio. The binding energies (BE) were referenced to the spurious C1s peak (284.6 eV) used as internal standard to take into account charging effects. The areas of the peaks were computed by fitting the experimental spectra to Gaussian/Lorentzian curves after removal of the background (Shirley function). Surface atom ratios were calculated from peak area ratios normalized by the appropriate atomic sensitivity factors [32].

A solar photoreactor based on Compound Parabolic Collectors (CPCs) installed at the Plataforma Solar de Almería (PSA) was employed to study the photodegradation of phenol under natural solar light; the characteristics of this reactor and the experimental set-up employed can be found elsewhere [3,33]. The total volume in the experiments was 35 L and the volume irradiated in the solar collector was 22 L. The starting conditions were the following: 50 mg/L of phenol, 500 mg/L of H_2O_2 and 200 mg/L of catalyst, added to the 10 L stirred tank; an initial pH value of ca. 6.5 was typically obtained under these conditions in the reactant dispersion. Evaluation of weather conditions required normalizing the intensity of the solar irradiance for experiments done in different days; irradiation was measured by means of a Kipp&Zonen CUV3 broadband UV radiometer with UV range (285–400 nm). It was inclined 37° (local latitude in PSA) and oriented to the south as the CPC photoreactor. A normalized illumination time defined elsewhere [34] was selected to normalize the solar irradiation. In this approach, the average solar UV flux on a perfect sunny day is considered to be 30 W_{UV} m^{-2}; accordingly, the irradiation time will be represented as $t_{30\,W}$ (Eq. (1)).

$$t_{30\,W,n} = t_{30\,W,n-1} + \Delta t_n \frac{UV}{30}\frac{V_i}{V_T} \quad (1)$$

The total organic content (TOC) of aqueous samples was determined with a Shimadzu TOC-5050A analyzer equipped with a Shimadzu ASI-5000A autosampler. Phenol or aromatic intermediates concentrations were monitored by High Performance Liquid Chromatography with UV detection (HPLC-UV), employing a nucleosil C-18 column at 50 °C and water/methanol at 65/35 ratio as mobile phase. The H_2O_2 content was measured by iodometric titration using KI 0.2 M, $Na_2S_2O_3$ 0.05 M and a starch indicator. Measurements of iron (II) and total iron lixiviates to the reaction medium were made by the 1,10-phenanthroline method (an adaptation of ISO 6332) by means of a UV–Vis Unicam-III spectrophotometer at 510 nm (maximum wave length of the iron–phenanthroline complex) and using a path length cuvette fixed in 5 cm, which multiplies the sensitivity of the technique.

3. Results and discussion

3.1. Catalysts characterization

Characterization results for some of the catalysts here examined were in part reported in previous contributions [3,27].

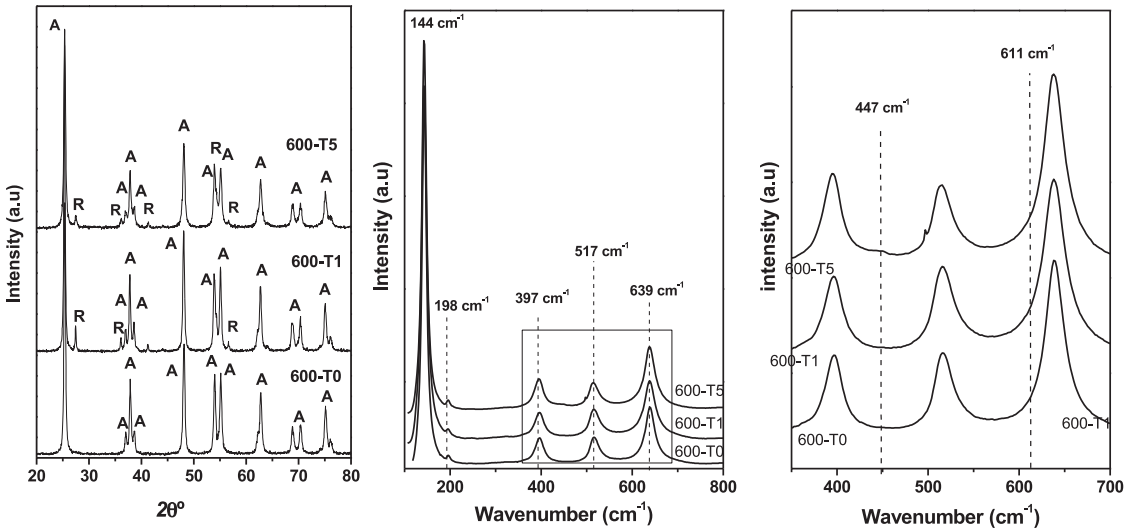

Fig. 1. Left: X-ray diffractograms of the indicated catalysts. Labels A and R correspond to peaks ascribed to anatase and rutile phases of titania, respectively. Middle: Raman spectra of the indicated samples. Right: detail of Raman spectra of the indicated samples, expanding the zone in which most intense peaks of rutile are detected (see main text).

Table 1
Main morphological/structural characteristics of the catalysts.

Catalyst	Crystal size[a] (nm)	Cell parameters[a] $a = b$, c (Å)	Cell volume[a] (Å^3)	Rutile%	Average particle size[b] (nm)	S_{BET}(m^2/g)
600-T0	24.7	3.78, 9.45	135.0	0	25.3	15.4
600-T1	30.0	3.78, 9.51	136.2	7.0	–	9.0
600-T5	22.5	3.78, 9.48	135.5	3.7	21.2	22.2

[a] For the major anatase phase of titania, from XRD results.
[b] From high resolution TEM pictures, considering Feret's diameters and volumetric average ($\sum n_i d_i^4 / \sum n_i d_i^3$).

Nevertheless, for the sake of self-consistency and completeness, full characterization results are compiled here. X-ray diffractograms and Raman spectra of the catalysts are displayed in Fig. 1. Table 1 summarizes main structural parameters derived from analysis of such results. In brief, the catalysts are basically constituted by the anatase form of titania (XRD peaks marked in Fig. 1 and Raman bands at ca. 144, 198, 397, 517 and 639 cm^{-1}, corresponding, respectively, to the $E_g(1)$, $E_g(2)$, $B_{1g}(1)$, $B_{1g}(2)+A_{2g}(1)$ and $E_g(3)$ modes expected for such a phase [35,36]). Additionally, the iron-containing catalysts display, in contrast to the undoped catalyst, the presence of relatively small XRD peaks corresponding to the presence of a minor rutile phase of titania in correlation with very weak Raman features at ca. 447 and 611 cm^{-1} (the latter basically inferred from the increased asymmetry in the anatase 639 cm^{-1} band in the presence of iron), corresponding to most intense E_g and A_{1g} modes expected for such phase [35]. This observation is in agreement with titania phase transformation to rutile being favoured in the presence of iron [37]. However, interestingly, the amount of rutile becomes maximized for the 600-T1 catalyst with lower iron content (Table 1). This must be related to the different degree of iron incorporation into the anatase lattice of titania, considering that phase transformation must be promoted in the presence of such lattice inserted transition metal cations [38]. This is also in agreement with previous analysis of catalysts of this kind, showing that iron incorporation to the anatase lattice becomes most favoured for iron contents close to 1 wt.% while iron

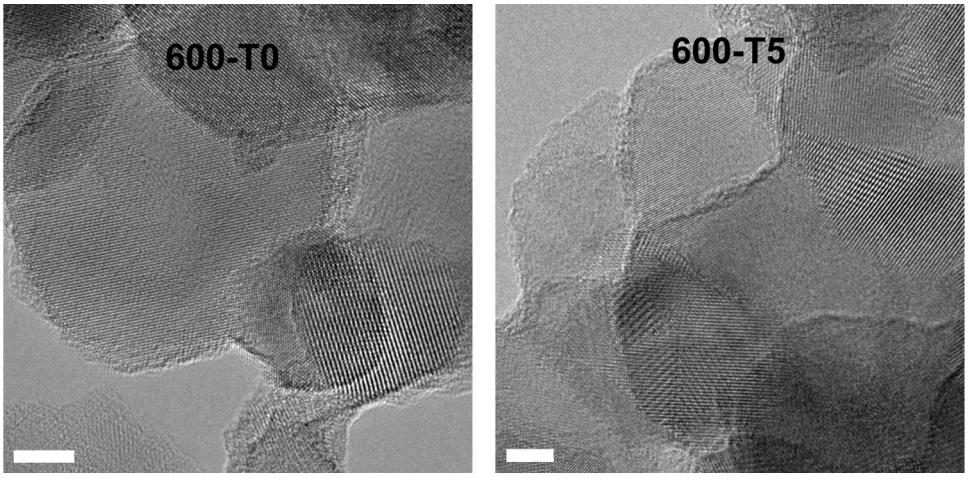

Fig. 2. Representative high resolution TEM pictures for the indicated catalysts. The scale corresponds to 5 nm in any case.

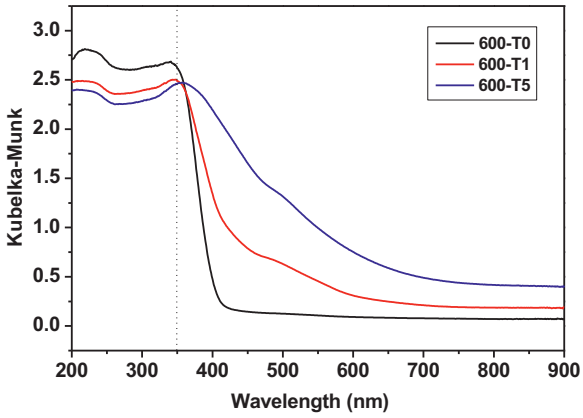

Fig. 3. UV–vis spectra for the indicated catalysts.

segregation is favoured above such content for catalysts prepared as here by sol–gel/microemulsion method [15]. Regarding the preparation pH, i.e. it becomes more acid as the iron concentration in the starting solution is increased, this can also favour higher iron segregation at the surface, as pointed out in a previous report [15]. The higher level of iron introduction into the anatase phase in 600-T1 with respect to 600-T5 is also supported by the respective degree of lattice expansion with respect to the undoped sample, according to data collected in Table 1 and taking into account previous investigation in this sense [15]. The structural/morphological differences are also reflected in specific surface area values (Table 1) which show that a higher sintering degree is produced for 600-T1, in fair correlation with crystal size evolutions and degree of lattice transformation to rutile. Further details on morphological characteristics of the catalysts have been obtained by TEM. As shown in Fig. 2, the catalysts are generally constituted by more or less spherical nanosized crystals (within particle aggregates in the micron size), displaying average sizes in qualitative agreement with XRD results (Table 1). In turn, a relatively higher dispersion in the size distribution is observed for the undoped catalyst (not shown).

No hint of iron containing phases was obtained from XRD, TEM or Raman results, which reveals a relatively high degree of dispersion for this component in any of the cases. Some details on the state of iron can be achieved from analysis of UV–vis spectra. As shown in Fig. 3, the undoped catalyst displays a steep increase of the absorption at wavelength lower than 380 nm (ca. 3.2 eV), attributed to the intrinsic band gap absorption of pure anatase TiO_2. The presence of iron produces additional absorptions in the visible region at energy below ca. 400 nm which increase as iron content increases, in consistency with the changes in the colour of the catalysts from white, for the undoped catalyst, to yellow and then light brown with higher iron loading. Apparently two components contribute to this enhanced absorption in the visible region. One can be attributed to the excitation of 3d electrons of Fe^{3+} to the TiO_2 conduction band (charge transfer transition) giving rise to a band centred at ca. 400 nm [15,28,39,40]. On the other hand, a band centred at ca. 500 nm is particularly apparent for the catalyst with highest iron content. This can be ascribed to the d-d transition of Fe^{3+} ($^2T_{2g} \rightarrow {}^2A_{2g}$, $^2T_{1g}$) or the charge transfer transition between interacting iron ions ($Fe^{3+} + Fe^{3+} \rightarrow Fe^{4+} + Fe^{2+}$) [15,28,39,40]. Correlation with EPR results in a previous work on catalysts prepared similarly than in this report (except for the calcination step) suggests that the band at ca. 500 nm can be related to the presence of aggregated oxidic iron entities [15], which, in accordance with discussion above on XRD results, prevail in 600-T5. In any case, it must be noted that it is not possible to differentiate between bulk or surface iron species on the basis of these results since both Fe-related bands appear similar for Fe-doped (bulk) or Fe-grafted (surface)

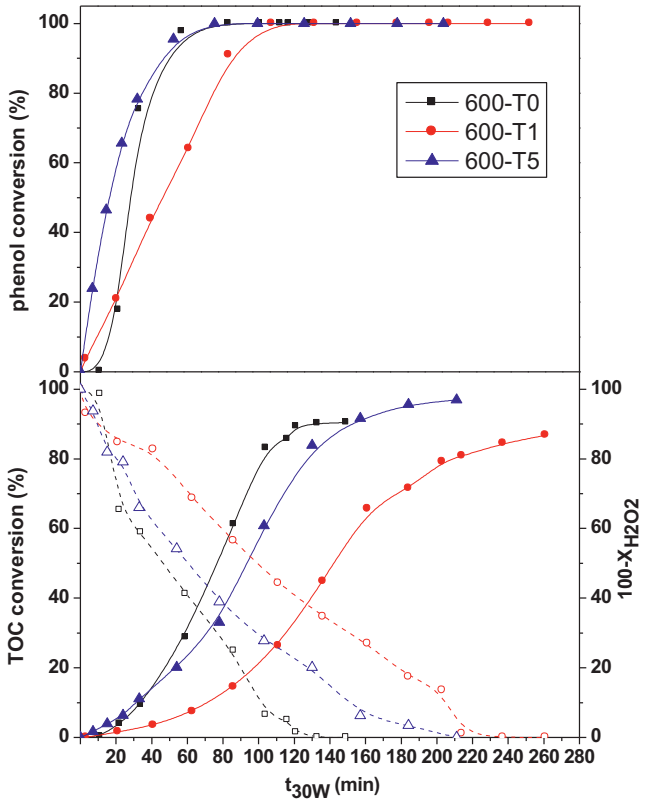

Fig. 4. Evolution of the TOC and phenol solar photodegradation (full symbols, solid lines) and H_2O_2 consumption (open symbols, dashed lines) over the indicated catalysts.

samples, their relative intensity being apparently a function of iron loading [10,11,15,28,39,40]. Nevertheless, recent analysis of the acidity of these samples by room temperature ammonia adsorption indicated lower pH with higher amount of iron (0.04, 0.09 and 0.21 mmol H^+ per gram of catalyst for 600-T0, 600-T1 and 600-T5, respectively [27]), thus supporting an important increase in the amount of surface iron species for 600-T5, in agreement with discussion above. On the other hand, as summarized in Table 2, XPS analysis of main peaks in Ti 2p and Fe 2p zones is consistent with values detected for Ti^{4+} cations in TiO_2 and Fe^{3+} species, respectively [39]. In turn, Fe/Ti atomic ratio values reveal an important degree of surface segregation of the iron in consistency with the presence of the band at ca. 500 nm in the UV–vis spectra (Fig. 3).

3.2. Photocatalytic properties

Fig. 4 shows the time-evolution curves for phenol and TOC conversions during solar photocatalytic degradation of phenol with H_2O_2. Phenol photolysis in the absence of solid catalyst can be considered nearly negligible since very slow phenol degradation with practically no change in TOC content was observed in the corresponding separate experiment (not shown). As inferred from Fig. 4, the photodegradation rate strongly depends on the amount of iron present in the catalyst, while relatively high phenol mineralization degrees are finally achieved in any case (92, 88 and 98% for the 600-T0, 600-T1 and 600-T5, respectively). It is worth noting that while the catalyst with ca. 1 at.% iron content exhibits the poorest photodegradation performance, an apparent improvement with respect to the undoped catalyst is observed for the catalyst with ca. 5 at.% of iron. Certain differences are detected in respective evolutions of phenol vs. TOC conversion between these latter two catalysts. This is reflected by evolutions observed

Table 2
XPS-derived surface characteristics and data for the main peaks detected in the iron-doped catalysts.

Catalyst	XPS binding energies (eV) of main peaks		Fe/Ti atomic ratio	
	Ti $2p_{3/2}$	Fe $2p_{3/2}$	Experimental	Theoretical
600-T1	457.9	710.5	0.021	0.01
600-T5	458.4	710.8	0.077	0.05

in aromatic intermediates during the course of the degradation process, somewhat more persistent over 600-T5 than over 600-T0, Fig. 5. This figure also shows that no phenol degradation activity is produced in the absence of solar light, which is admitted to the reactor about 30 min after starting the experiment. On the whole, comparing 600-T5 and 600-T0, the results reveal that while first steps of phenol degradation are faster in 600-T5, intermediate or final steps leading to final mineralization are somewhat faster in the absence of iron, suggesting a different nature for active sites or reaction mechanism in each case. This is in agreement with the presence of new Fe-related active sites in 600-T5 which would individually present a relatively lower oxidizing power. These may well correspond to photogenerated holes (or hole-derived species) in the localized narrow band derived from Fe^{3+} whose oxidizing power is expected to be lower than that of corresponding holes (or hole-derived species) in the valence band of TiO_2 [11,28]. Results in Fig. 5 also reveal that catechol, p-benzoquinone and hydroquinone are in any case formed as primary oxidation intermediates resulting from phenol hydroxylation. The fact that, among the three intermediates, catechol is the one displaying highest concentration can be in part due to the relatively high rate of •OH radical generation in the presence of H_2O_2, which contributes to ortho-hydroxylation of the aromatic ring during the photocatalytic process [41,42]; we cannot however discard that catechol predominates because of its relatively higher stability among possible intermediates formed. In any case, it is worth considering that concentrations of hydroquinone and p-benzoquinone as well as catechol become negligible in the three examined cases after 3 h; it must be taken into account that some of these compounds (particularly the hydroquinone and p-benzoquinone) are by far the most toxic intermediates produced during the oxidation route of phenol [43].

The results obtained contrast with results in the literature generally displaying a decrease in the phenol photodegradation rate with increasing the iron content of the catalyst or alternatively (depending also on specific conditions like the solution pH) displaying a maximum at iron contents relatively low around 0.5–1.0 at.% [10,13,16,27], similar to that of 600-T1. Indeed, our previous investigation on catalysts of this type (calcined at 450 °C, after which only anatase nanocrystals with residual brookite phase were observed in both doped and undoped specimens) for phenol photodegradation employing UV light and oxygen as oxidant at laboratory scale exhibited maximum activity for iron content around 1.0 at.% when working at acid pH. As exposed above, such iron content apparently maximizes the iron incorporation to the anatase lattice (and/or, simultaneously, iron segregation at the surface, forming less active oxide entities [10,44], becomes minimized) [15].

The situation can however be more complex when H_2O_2 is the oxidant because of difficulties to establish optimum experimental conditions in terms of avoiding to a maximum hydroxyl scavenging effects and/or formation of inactive surface peroxo complexes upon interaction with H_2O_2 [18]. Indeed, previous experiments on the same series of catalysts but calcined at 450 °C (and tested at laboratory scale employing UV light) showed a significant hindering of the phenol photodegradation activity as a consequence of mentioned H_2O_2 scavenging effect [18]. However, in the present case, no important differences are detected between the catalysts in H_2O_2 scavenging of holes despite the fact that some level of H_2O_2 self-scavenging can apparently occur in all cases below a certain TOC conversion degree, according to results presented in Fig. 6.

As mentioned above, the differences detected in the photoactivity obtained as a function of the iron loading cannot be directly justified on the basis of the structural/chemical properties

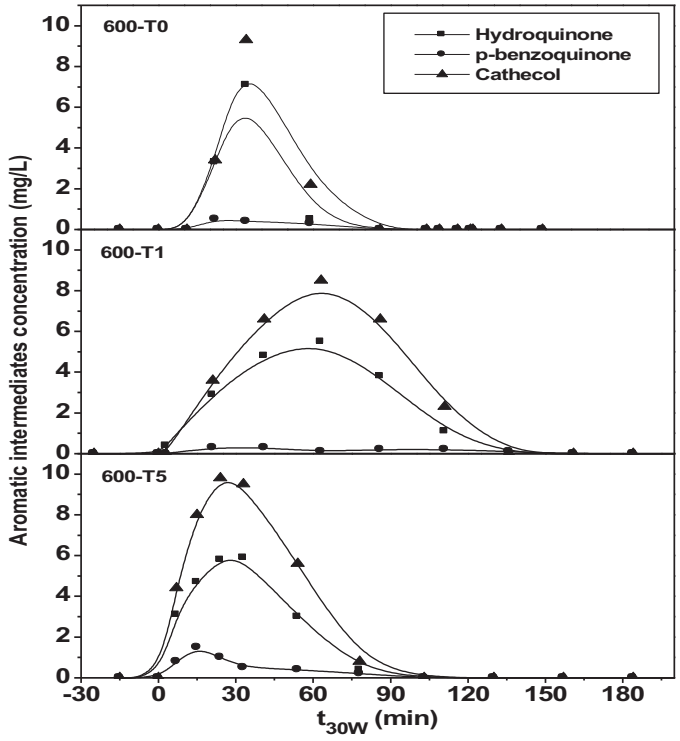

Fig. 5. Evolution of aromatic intermediates formed during the solar photodegradation of phenol over the indicated catalysts.

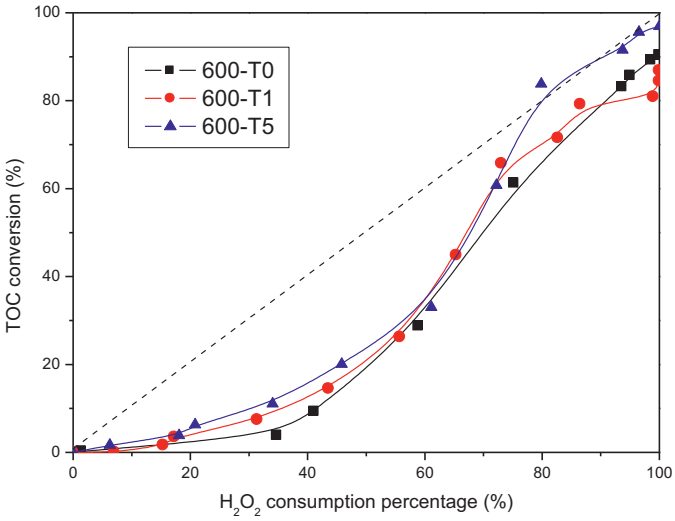

Fig. 6. TOC conversion as a function of H_2O_2 consumption percentage for the indicated catalysts.

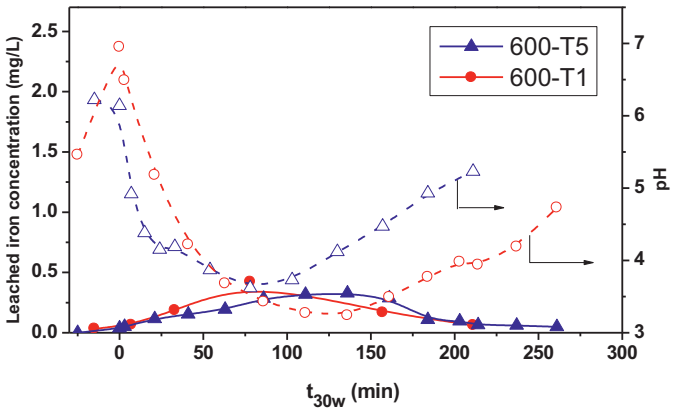

Fig. 7. Evolution of total iron lixiviated from the doped catalysts (solid lines, full symbols) and pH (dashed lines, open symbols) during the solar photodegradation of phenol over the indicated catalysts.

of the catalysts provided by characterization of the initial catalysts. According to previous results on catalysts of this series but (as final step of the preparation) calcined at 450 °C [15,18], and as usually found in the scientific literature [10,17], the phenol photodegradation activity in Fe-doped samples shows either a maximum for a doping level about 1 at.% or monotonously decreases with the iron loading. Thus, if 600-T1 with about 1 at.% loading (and at neutral pH) displays, as observed in Fig. 4, a decrease in the photoactivity with respect to the undoped sample, a further decrease would have been expected for 600-T5. Indeed, a decrease in the phenol photodegradation activity upon increasing the iron loading was observed previously in this same series of catalysts (although calcined at 450 °C) when operating, at natural pH close to neutral one and using UV as exciting light in a laboratory reactor [18]. Explanations given for that behaviour are based on the fact that, notwithstanding some doubts could exist for optimum Fe doping level, the presence of surface segregated iron oxide type particles always result detrimental to the activity since they can provide a mechanism in which electron–hole recombination predominate [10,15]. In our case, according to characterization results described above, such surface segregated iron oxide type particles apparently increase with the iron loading and therefore a decrease in the photodegradation activity with the iron loading would have been expected.

However, another relevant factor is observed for the Fe-containing samples in the solar-light experiments here presented (as well as for those performed under different experimental conditions, i.e. using O_2 from air as oxidant, or for catalysts calcined at 450 °C in which basically only anatase titania phases are present [17,27]) as a difference with experiments performed under laboratory conditions with UV light [15,18]. This is related to the fact that appreciable amounts of iron lixiviates to the liquid phase are observed to be produced, as shown in Fig. 7. Such leached iron is shown to appear in the form of Fe(II) species in the reactant solution. The overall amount of iron undergoing such phenomenon is relatively large, ca. 23 and 4.7% of the whole iron amount present in each case for 600-T1 and 600-T5 catalysts, respectively; it may be noted that the amount of iron lixiviates produced in this case is however lower than that detected in the catalysts of the same series calcined at 450 °C under similar conditions [17], thus revealing a higher structural stability of iron oxide species as the calcination temperature is increased. The evolution of the iron concentration during the course of the reaction shows that final readsorption of the whole iron on the surface of the catalyst is produced. On the other hand, fair correlation between the evolution of leached iron concentration and the pH in the reactant solution is observed (Fig. 7). This can be explained by the fact that iron leaching is produced as a consequence of the interaction of the catalyst with short-chain organic acids produced as intermediates during the decomposition of phenol or other aromatic intermediates, as confirmed in recent works [17,27], and in agreement with previous proposal [25]. And, as mentioned, such iron leaching process does not appear to be produced when operating with this type of catalysts under laboratory conditions employing UV light (high-pressure Hg lamp of 500 W with an emission range between 260 and 420 nm, with an intense emission band centred at 366 nm [15,18]). Although we cannot fully discard other factors to explain such differences (type of reactor, reaction conditions employed in each case like the type of stirring, way of irradiating, amount of O_2 dissolved, etc.) the different energy of the exciting light employed in each case can play an important role, i.e. solar light can excite energy levels – either derived from the iron dopant or intrinsic defects of the TiO_2 itself [1,10–12,28] – in the TiO_2 bandgap with a lower oxidation power than UV light. Such lower oxidation power can favour the formation of partial oxidation products. Under such conditions, the lifetime of short chain organic acids responsible of the leaching process would be most likely appreciably longer than when exciting with UV light.

The fact that iron becomes lixiviated to the reaction medium opens the possibility that some contribution from homogeneous photo-oxidation or related processes (for instance, considering the presence of H_2O_2, photo-Fenton type processes) could take place, even in combination with photocatalysis by the solid itself [45]. However, it can be noted that maximum amounts of iron lixiviates are produced when the concentration of H_2O_2 has decreased to more than half its initial concentration. In addition, the maximum amount of iron detected in the liquid homogeneous phase is relatively low (1.5 mg/L, Fig. 7) and, as mentioned, in the form of mainly Fe(II) species, which would rapidly be converted in Fe^{3+} by H_2O_2 that undergo photo-Fenton [46]; it must be noted in this sense that 1.5 mg/L is a rather low concentration of iron which would require appreciably longer times for phenol photomineralization through homogeneous photo-Fenton (and using the same solar photoreactor than in the present work) than observed here [46]. Besides, pH between 3.5 and 6 is not the optimal for homogeneous photo-Fenton.

An alternative to explain the activity of the iron-containing samples when lixiviated iron is observed to be produced was recently proposed [17,27], on the basis of previous proposal by Araña et al. [25]. Considering the mentioned correlation between amounts of lixiviated iron and formation of short chain organic acids (reflected by pH decrease, Fig. 7), iron can be extracted from the catalysts through previous formation of Fe–carboxylic acid complexes [25,27]. Such surface iron–carboxylic acid complexes can act as photoactive species which strongly favour the photodecomposition of phenol or other organic molecules derived from it through partial oxidation processes. Final readsorption of the iron on the sample surface (Fig. 7) can be related to posterior precipitation of Fe^{3+} species (with relatively low solubility) formed upon interaction of the decarboxylated Fe^{2+} species with photogenerated holes or through oxidation with H_2O_2 [25,27], a process which leaves the catalyst ready for the next catalytic cycle.

Another explanation for the observed enhanced photoactivity in the presence of iron (600-T5 catalyst) could simply be related to the activity of the new surface iron–carboxylic acid complexes themselves, as recently proposed for Fe-grafted samples in which such iron leaching was not apparently detected [11,28]. The observed iron-leaching phenomena would then just be a side effect and the leached iron species would then just be spectators in the whole process. A new experiment was specifically designed in order to check for this possibility while additionally exploring differences between O_2 and H_2O_2 as oxidants in the absence of H_2O_2

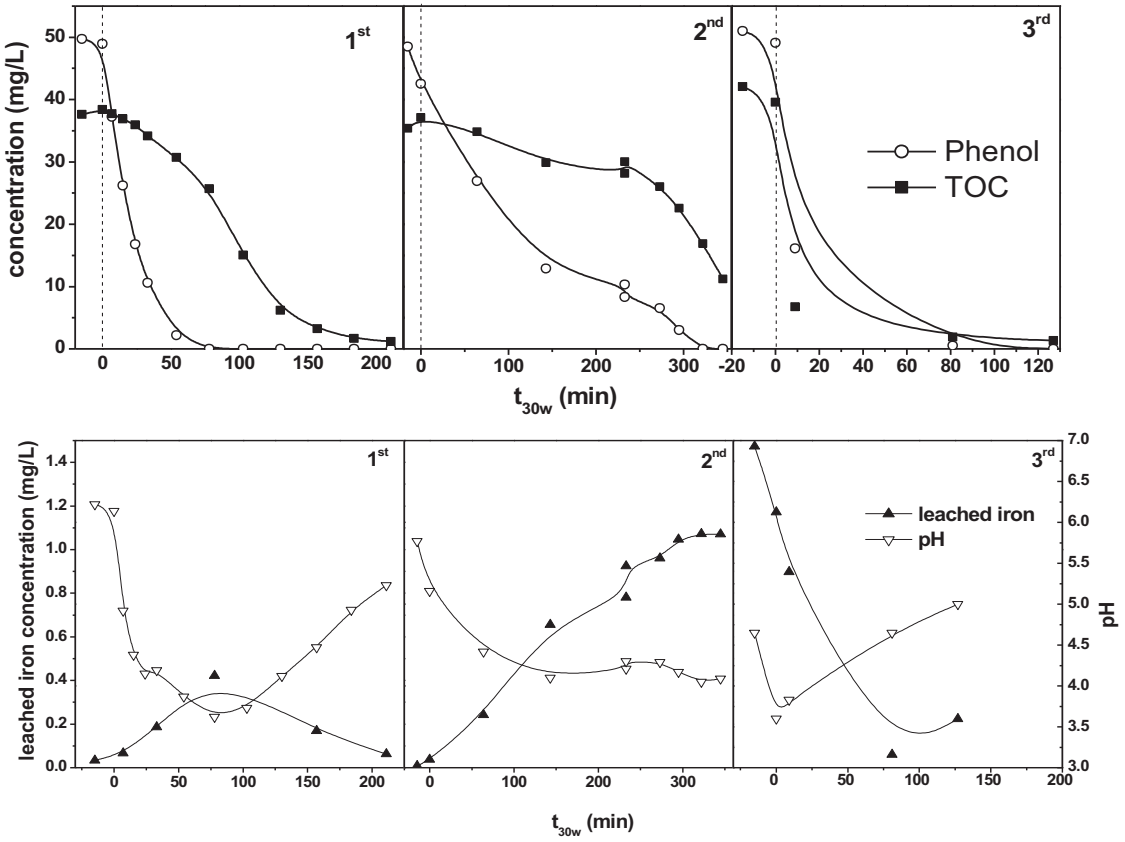

Fig. 8. Evolutions of phenol and TOC concentrations, total iron lixiviated and pH during consecutive phenol photooxidation experiments over 600-T5. The initial phenol concentration is 50 mg/L in the three runs. H_2O_2 initial concentrations of 500 mg/L are used in runs 1st and 3rd while no H_2O_2 was added in run 2nd. The rest of conditions are as specified in main text.

self-scavenging phenomena, according to results in Fig. 6. Thus, as displayed in Fig. 8, a series of three consecutive runs have been carried out with 600-T5. The first run is similar to the one presented in Fig. 4, the reaction being carried out until all TOC and H_2O_2 are consumed. Then, 50 mg/L of phenol are added to the tank and no H_2O_2 is added, i.e. atmospheric air acts as oxidant. In such case, phenol photodegradation is observed to be much slower, in agreement with comparison with previous experiments performed under similar conditions in which oxygen from air was used as oxidant [27]. Under these conditions leached iron did not precipitate again at the end of the treatment as pH remained low while carboxylic acid intermediates were not finally mineralized due to the mild conditions (only oxygen) of the treatment. The second run was stopped when all phenol has been consumed but iron lixiviated to the solution is in a maximum around 1 mg/L (actually slightly higher when starting 3rd run since a little bit more became lixiviated between runs being pH around 4); i.e. with a lower concentration of surface iron. Then, phenol and H_2O_2 are reintroduced in the tank. A faster overall consumption of phenol and TOC is observed upon irradiating during this third run due to homogeneous photo-Fenton than when starting with the whole iron in the catalyst (Fig. 4). In this case the pH increased and iron became readsorbed as in first run. This suggests either that the leaching/readsorption process itself might be not directly involved in the reaction mechanism (being then only a side effect) or that an optimum concentration of iron at the surface is produced as a consequence of the leaching process, in line with recent proposals showing a saturation level for the photoactive surface iron in Fe-grafted samples [28,47]. Further experiments would be however required to explore this issue.

A final question concerns explaining differences between catalytic performances of 600-T1 and 600-T5, provided that iron leaching is produced to a similar extent in both cases (Fig. 7). Such difference suggests a relevant role for the solid catalyst itself. As inferred from characterization results, differences between both catalysts are related to the level of iron doping achieved in each case in the form of iron incorporated to the titania lattice, which is higher for 600-T1. It may then occur that such incorporated iron basically act as electron–hole recombination centres which prevail during light handling within the balance with possible beneficial effects provided by the formation of surface iron complexes similar to those postulated to act as active centres in 600-T5. It must be noted in any case that beneficial effects of iron doping on the photoactivity typically appear when dealing with titania samples of relatively small crystal size (below about 10 nm) [10,15,28,48], which has been recently related to the fact that they could maximize contributions from (dopant-derived) surface photoactive species [28]. We cannot in any case discard that the photocatalytic properties of the doped titania in our samples with larger crystal size, or of the anatase/rutile heterostructure present in the Fe-doped samples (Fig. 1 and Table 1), become optimized at doping levels lower than that found for smaller titania crystals (which, as mentioned above, is close to the loading employed in 600-T1) and that 600-T5 is then closer to that optimum doping level. Another contribution to the decreased activity of 600-T1 could be related to its lower specific surface area associated to its higher crystallinity and rutile formation (Table 1). This could favour a lower hydroxylation degree at its surface, which would be detrimental in terms of charge separation; it must be considered in this sense that hydroxyl groups act as main hole traps giving rise to hydroxyl radicals, which are likely the most active species in phenol or other intermediates oxidation reactions under the employed conditions [29]. Another factor like differences in surface acid/base properties is discarded to explain

the lowest activity shown by 600-T1 since, as mentioned above, the surface acidity, whose increase can favour phenol photooxidation activity [15,30], increases with the amount of iron.

4. Conclusions

Titania and iron-doped titania photocatalysts prepared by sol–gel/microemulsion and calcined at 600 °C have been tested with respect to their activity for phenol photodegradation employing hydrogen peroxide as oxidizing agent under solar irradiation at pilot plant scale. Opposite to results generally obtained in the literature, in which optimum photocatalytic properties are achieved upon doping at a relatively weak level (around 1 at.%), it is observed that the catalyst with a relatively high iron loading (5 at.%) displays phenol photodegradation activity similar or slightly higher than the undoped sample while the weakly doped system (with 1 at.%) displays poorest performance. Such particularities are explained on the basis of the existence of formation of new photoactive centres at the surface of the catalyst. These are proposed to result from interaction of surface iron species with short-chain carboxylic acids formed during the course of the reaction as a consequence of phenol (or other aromatic intermediates) partial oxidation processes. Such phenomenon is evidenced by observation of iron lixiviation (appearing in the form of Fe(II) species in the reaction solution) typically associated to such type of interaction. Posterior readsorption of the iron on the catalyst surface is also observed and attributed to oxidation of the lixiviated iron species to less soluble Fe(III). Photoactivity differences as a function of the iron loading are also correlated to the specific characteristics of the nanostructure present in each case (on the basis of characterization results), which show that iron incorporation to the titania lattice becomes maximized for the sample with 1 at.% Fe. Prevalence of electron–hole recombination centres during solar light handling in such case is proposed to result detrimental to its photoactivity. Finally, as expected, H_2O_2 is shown to be a more efficient oxidant than O_2 from air for the photodegradation process provided effects of self-scavenging of hydroxyl radicals by H_2O_2 become adequately controlled.

Acknowledgements

Thanks are due to the MEC (projects CTQ2004-03409/BQU, CTQ2006-15600/BQU and CTM2010-14883) and CSIC (project PIF 200420F0280) and Programa de Acceso de Grandes Instalaciones Científicas Españolas GIC-05-17, for financial support. Support from EU COST Action CM1104 is also acknowledged. We would also like to thank ICP-CSIC Unidad de Apoyo staff for performing a part of the textural analysis and spectroscopic results, as well as Dr. Laura Pascual for performing the TEM experiments and Prof. J.L.G. Fierro for performing XPS measurements as well as the technical assistance of Agustín Carrión at the PSA.

References

[1] M.R. Hoffmann, S.T. Martin, W. Choi, D. Bahnemann, Chemical Reviews 95 (1995) 69.
[2] M.A. Henderson, Surface Science Reports 66 (2011) 185.
[3] C. Adán, A. Bahamonde, A. Martínez-Arias, M. Fernández-García, L.A. Pérez-Estrada, S. Malato, Catalysis Today 129 (2007) 79.
[4] S. Ikeda, B. Ohtani, Physical Chemistry Chemical Physics 5 (2003) 778.
[5] R.R. Ozer, J.L. Ferry, Environmental Science & Technology 35 (2001) 3242.
[6] M. Pelaez, N.T. Nolan, S.C. Pillai, M.K. Seery, P. Falaras, A.G. Kontos, P.S.M. Dunlop, J.W.J. Hamilton, J.A. Byrne, K. O'Shea, M.H. Entezari, D.D. Dionysiou, Applied Catalysis B 125 (2012) 331.
[7] A. Fuerte, M.D. Hernández-Alonso, A.J. Maira, A. Martínez-Arias, M. Fernández-García, J.C. Conesa, J. Soria, Chemical Communications (2001) 2178.
[8] G. Colón-Ibáñez, C. Belver-Coldeira, M. Fernández-García, in: J.A. Rodríguez, M. Fernández-García (Eds.), Synthesis, properties and applications of oxide nanomaterials, John Wiley and Sons, New Jersey, 2007, pp. 491–562.
[9] R.I. Bickley, J.S. Lees, R.J.D. Tilley, L. Palmisano, M. Schiavello, Journal of the Chemical Society, Faraday Transactions 88 (1992) 377.
[10] M. Litter, J. Navío, Journal of Photochemistry and Photobiology A 98 (1996) 171 (and references therein).
[11] H. Yu, H. Irie, Y. Shimodaira, Y. Hosogi, Y. Kuroda, M. Miyauchi, K. Hashimoto, Journal of Physical Chemistry C 114 (2010) 16481.
[12] M. Nishikawa, Y. Mitani, Y. Nosaka, Journal of Physical Chemistry C 116 (2012) 14900.
[13] E. Piera, M.I. Tejedor-Tejedor, M.E. Zorn, M.A. Anderson, Applied Catalysis B 46 (2003) 671.
[14] J. Navío, G. Colón, M. Macías, C. Real, M. Litter, Applied Catalysis A 177 (1999) 111.
[15] C. Adán, A. Bahamonde, M. Fernández-García, A. Martínez-Arias, Applied Catalysis B 72 (2007) 11.
[16] K.T. Ranjit, B. Viswanathan., Journal of Photochemistry and Photobiology A 108 (1997) 79.
[17] C. Adán, J. Carbajo, A. Bahamonde, I. Oller, S. Malato, A. Martínez-Arias, Applied Catalysis B 109 (109) (2011) 168.
[18] C. Adán, J. Carbajo, A. Bahamonde, A. Martínez-Arias, Catalysis Today 143 (2009) 247.
[19] T. Velegraki, D. Mantzavinos, Chemical Engineering 140 (2008) 15.
[20] A.A. Yawalkar, D.S. Bhatkhande, V.G. Pangarkar, A.A.C.M. Beenackers, Journal of Chemical Technology and Biotechnology 76 (2001) 363.
[21] B. Tryba, International Journal of Photoenergy (2008) 721824.
[22] C.G. Silva, J.L. Faria, Journal of Molecular Catalysis A 305 (2009) 147.
[23] B. Tryba, A.W. Morawski, M. Inagaki, M. Toyoda, Applied Catalysis B 63 (2006) 215.
[24] J. Carbajo, C. Adán, A. Rey, A. Martínez-Arias, A. Bahamonde, Applied Catalysis B 102 (2011) 85.
[25] J. Araña, O. González Díaz, J.M. Rodríguez, J.A. Herrera Melián, C. Garriga i Cabo, J. Pérez Peña, M. Carmen Hidalgo, J.A. Navío-Santos, J. Mol. Catal. A 197 (2003) 157.
[26] W.Y. Teoh, R. Amal, L. Mädler, S.E. Pratsinis, Catalysis Today 120 (2007) 203.
[27] C. Adán, A. Martínez-Arias, S. Malato, A. Bahamonde, Applied Catalysis B 93 (2009) 96.
[28] H. Tada, Q. Jin, H. Nishijima, H. Yamamoto, M. Fujishima, S. Okuoka, T. Hattori, Y. Sumida, H. Kobayashi, Angewandte Chemie International Edition 50 (2011) 3501.
[29] A. Sclafani, L. Palmisano, M. Schiavello, Journal of Physical Chemistry 94 (1990) 829.
[30] A. Testino, I.R. Bellobono, V. Buscaglia, C. Canevali, M. D'Arienzo, S. Polizzi, R. Scotti, F. Morazzoni, Journal of the American Chemical Society 129 (2007) 3564.
[31] H. Zhang, J.F. Banfield, Journal of Physical Chemistry B 104 (2000) 3481.
[32] C.D. Wagner, L.E. Davis, M.V. Zeller, J.A. Taylor, R.H. Raymond, L.H. Gale, Surface and Interface Analysis 3 (1981) 211.
[33] M. Kositzi, A. Antoniadis, I. Poulios, I. Kiridis, S. Malato, Solar Energy 77 (2004) 591.
[34] M. Hincapié Pérez, G. Peñuela, M.I. Maldonado, O. Malato, P. Fernández-Ibáñez, I. Oller, W. Gernjak, S. Malato, Applied Catalysis B 64 (2006) 272.
[35] H. Cheng, J. Ma, Z. Zhao, L. Qi, Chemistry of Materials 7 (1995) 663.
[36] M. Fernández-García, A. Martínez-Arias, A. Fuerte, J.C. Conesa, Journal of Physical Chemistry B 109 (2005) 6075.
[37] Y. Lida, S. Ozaki, Journal of the American Ceramic Society 44 (1961) 120.
[38] P.M. Rao, B. Viswanathan, R.P. Viswanathan, Journal of Materials Science 30 (1995) 4980.
[39] J. Zhu, F. Chen, J. Zhang, H. Chen, M. Anpo, Journal of Photochemistry and Photobiology A 180 (2006) 196.
[40] N. Serpone, D. Lawless, J. Disdier, J.-M. Hermann, Langmuir 10 (1994) 643.
[41] J.A. Zazo, J.A. Casas, A.F. Mohedano, M.A. Gilarranz, J.J. Rodríguez, Environmental Science & Technology 39 (2005) 9295.
[42] A. Rey, M. Faraldos, J.A. Casas, J.A. Zazo, A. Bahamonde, J.J. Rodríguez, Applied Catalysis B 86 (2009) 69.
[43] A. Santos, P. Yustos, S. Rodríguez, F. García-Ochoa, Applied Catalysis B 65 (2006) 269.
[44] J. Bandara, J.A. Mielczarski, A. Lopez, J. Kiwi, Applied Catalysis B 34 (2001) 321.
[45] H. Kim, J. Lee, H. Lee, C. Lee, Applied Catalysis B 115/116 (2012) 219.
[46] M. Hincapie, M.I. Maldonado, I. Oller, W. Gernjak, J.A. Sánchez-Pérez, M.M. Ballesteros, S. Malato, Catalysis Today 101 (2005) 203.
[47] N. Murakami, A. Ono, M. Nakamura, T. Tsubota, T. Ohno, Applied Catalysis B 97 (2010) 115.
[48] W. Choi, A. Termin, M.R. Hoffmann, Angewandte Chemie International Edition 33 (1994) 1091.